



HAL
open science

Magnetic minerals in three Asian rivers draining into the South China Sea: Pearl, Red, and Mekong Rivers

Catherine Kissel, Zhifei Liu, Jinhua Li, Camille Wandres

► **To cite this version:**

Catherine Kissel, Zhifei Liu, Jinhua Li, Camille Wandres. Magnetic minerals in three Asian rivers draining into the South China Sea: Pearl, Red, and Mekong Rivers. *Geochemistry, Geophysics, Geosystems*, 2016, 17 (5), pp.1678-1693. 10.1002/2016GC006283 . hal-03118199

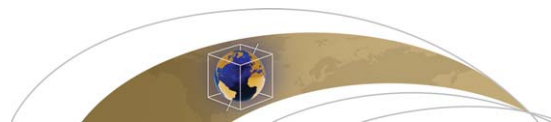
HAL Id: hal-03118199

<https://hal.science/hal-03118199>

Submitted on 22 Jan 2021

HAL is a multi-disciplinary open access archive for the deposit and dissemination of scientific research documents, whether they are published or not. The documents may come from teaching and research institutions in France or abroad, or from public or private research centers.

L'archive ouverte pluridisciplinaire **HAL**, est destinée au dépôt et à la diffusion de documents scientifiques de niveau recherche, publiés ou non, émanant des établissements d'enseignement et de recherche français ou étrangers, des laboratoires publics ou privés.



RESEARCH ARTICLE

10.1002/2016GC006283

Magnetic minerals in three Asian rivers draining into the South China Sea: Pearl, Red, and Mekong Rivers

Catherine Kissel¹, Zhifei Liu², Jinhua Li³, and Camille Wandres¹

¹Laboratoire des Sciences du Climat et de l'Environnement/IPSL, CEA-CNRS-UVSQ, Université Paris-Saclay, Gif-sur-Yvette Cédex, France, ²State Key Laboratory of Marine Geology, Tongji University, Shanghai, China, ³Key Laboratory of Earth and Planetary Physics, Institute of Geology and Geophysics, Chinese Academy of Sciences, Beijing, China

Key Points:

- Magnetic properties of sediments from three main Asian rivers compared to clay mineralogy and major element content
- Intra and interbasin variations with variable proportions of sedimentary hematite versus magnetite
- Signal transferred to the sea related to the geology of the catchment and to the weathering/erosion balance

Supporting Information:

- Supporting Information S1
- Table S1

Correspondence to:

C. Kissel,
Catherine.Kissel@lsce.ipsl.fr

Citation:

Kissel, C., Z. Liu, J. Li, and C. Wandres (2016), Magnetic minerals in three Asian rivers draining into the South China Sea: Pearl, Red, and Mekong Rivers, *Geochem. Geophys. Geosyst.*, 17, 1678–1693, doi:10.1002/2016GC006283.

Received 28 JAN 2016

Accepted 6 APR 2016

Accepted article online 8 APR 2016

Published online 8 MAY 2016

Abstract The use of the marine sedimentary magnetic properties, as tracers for changes in precipitation rate and in oceanic water masses transport and exchanges, implies to identify and to characterize the different sources of the detrital fraction. This is of particular importance in closed and/or marginal seas such as the South China Sea. We report on the magnetic properties of sedimentary samples collected in three main Asian rivers draining into the South China Sea: the Pearl, Red, and Mekong Rivers. The geological formations as well as the present climatic conditions are different from one catchment to another. The entire set of performed magnetic analyses (low-field magnetic susceptibility, ARM acquisition and decay, IRM acquisition and decay, back-field acquisition, thermal demagnetization of three-axes IRM, hysteresis parameters, FORC diagrams, and low-temperature magnetic measurements) allow us to identify the magnetic mineralogy and the grain-size distribution when magnetite is dominant. Some degree of variability is observed in each basin, illustrating different parent rocks and degree of weathering. On average it appears that the Pearl River is rich in magnetite along the main stream while the Mekong River is rich in hematite. The Red River is a mixture of the two. Compared to clay mineral assemblages and major element contents previously determined on the same samples, these new findings indicate that the magnetic fraction brings complementary information of great interest for environmental reconstructions based on marine sediments from the South China Sea.

1. Introduction

Over the last decades, environmental magnetic studies have been developed in marine and continental realms along with the progresses in the laboratory techniques. Magnetic minerals are ubiquitous and they are potential proxies for paleoclimatic and paleoceanographic reconstructions, for understanding sediment transport processes and characterizing anthropogenic pollution [Evans and Heller, 2003]. For example, combined with other detrital tracers (granulometry, clay mineralogy), magnetic properties, which can be measured rapidly, economically and nondestructively, allowed to reconstruct past changes in deep oceanic circulation [Kissel et al., 1999, 2009, 2013; Mazaud et al., 2007]. These studies were conducted in large, open oceans where the source of magnetic minerals is unique and well identified. In other smaller oceanic basins, surrounded by various terrestrial environments, such as the South China Sea (SCS), the first step is to precisely characterize the composition of the terrigenous sediment delivered at sea by the neighboring continental regions.

The climate of Southeast Asia is largely dominated by the monsoon regime, an extremely important and sensitive component of the climatic system, resulting from seasonal differences in the atmospheric pressure and temperature gradients between ocean and land. The Indo-Asian monsoon is divided into a warm and wet summer monsoon and a cold and dry winter monsoon [An et al., 2015 and references therein]. In summer, SE winds carry moist air from the Indian Ocean to East Asia. The timing, the length, and the intensity of the rainy season is variable from south to north in this large area extending in latitude from about 5°S to about 25°N [Wang et al., 2004 and references therein]. The amount and the composition of the terrigenous fraction may therefore change on the regional scale not only because the eroded/weathered parent rocks differ in composition but also because of the variety of climatic conditions.

The East-Asian fluvial system draining into the SCS is among the most active ones in the world in terms of detrital discharge with the highest denudation rates [Summerfield and Hulton, 1994; Milliman and Farnsworth, 2011]. The three main active rivers collecting the continental waters and supplying an enormous

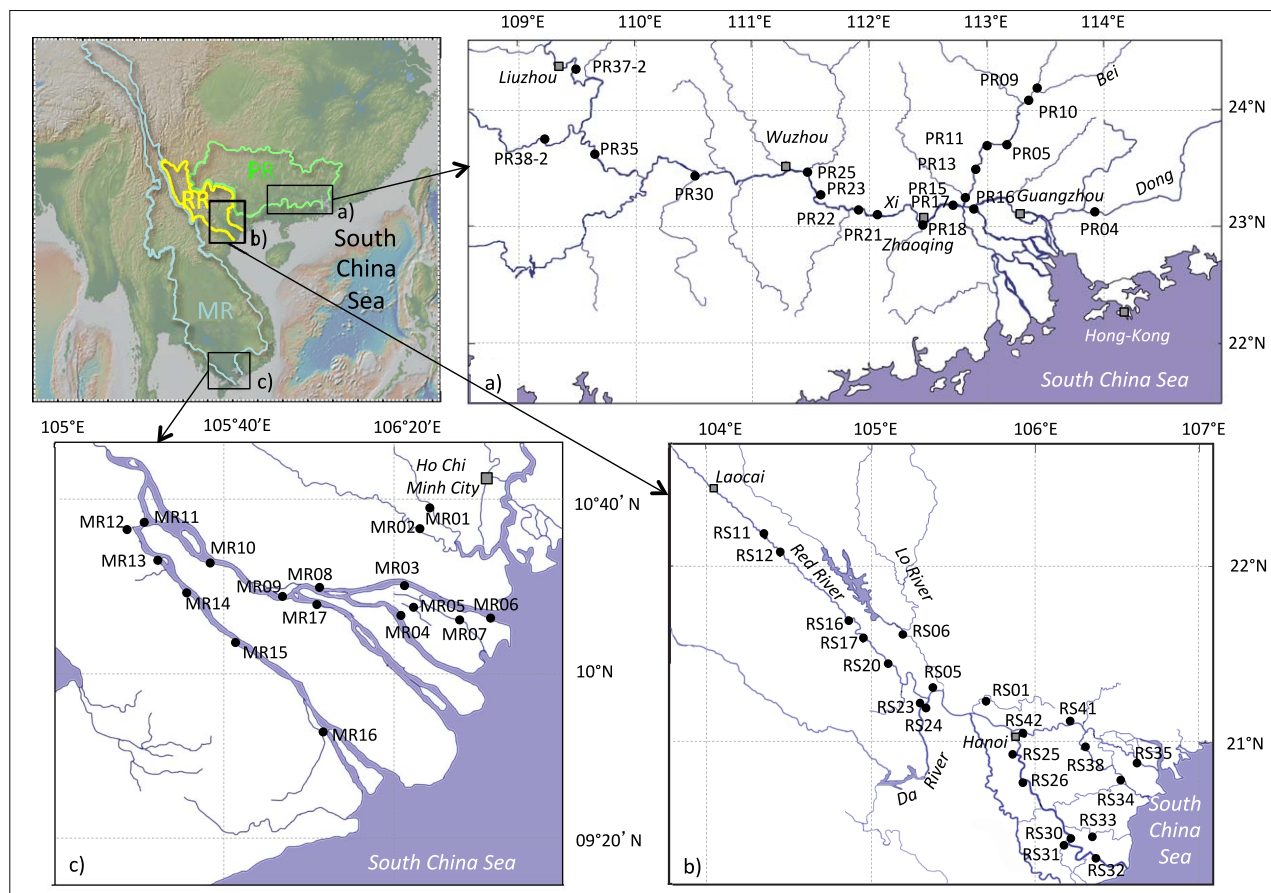


Figure 1. Schematic maps of the three rivers showing the location of the studied sites. (a) Pearl River; (b) Red River; and (c) Mekong River. The three catchments are localized in the small general map in the left top corner.

amount of sediment to the SCS are the Pearl River, the Red River, and the Mekong River [Liu and Stettegger, 2014; Liu *et al.*, 2016, and references therein]. They have very large drainage areas over the Asian continent and they end in the north, the center, and the south of the SCS, respectively. The detrital sediments they transport are potential tracers of the environmental/climatic conditions affecting the continent and, after they are delivered to the sea, of the oceanic circulation at different depths. Any reconstruction of (paleo)environmental/(paleo)oceanographic changes in this area first requires a precise characterization of the composition of the terrigenous sediment transported by each of these fluvial systems (Figure 1).

Analyses of different proxies including magnetic ones have been conducted off the river deltas, in the SCS. Recently, magnetic grain size of samples from the subaqueous delta of the Red River has been compared to grain size of river samples [Nguyen *et al.*, 2016]. Only one exhaustive study combining major and trace elements, clay mineralogy and assemblages, and Nd, Sr isotopes has been so far conducted in sediments deposited along the streams and at the river mouths of the three rivers [Liu *et al.*, 2007, 2016]. It has shown a large variety of compositions interpreted in terms of differences in the relative contribution of erosion and weathering [Liu *et al.*, 2007, 2016]. Here we report on the study of the magnetic properties of the same sediments collected in the three rivers. Indeed, magnetic mineralogy may yield complementary information regarding the local and/or regional origin and nature of the transported detrital material.

2. River Settings

The Pearl River is an extensive fluvial system extending west-east in southern China (Figure 1a). It is the third largest river in China with a delta located in the northern part of the SCS [Clark *et al.*, 2004]. It is made of the coalescence of the three watersheds of the west, north and east rivers. The western branch, Xijiang,

is the longest one (2400 km) and it is the main contributor to the Pearl River delta. The other two main branches (Beijiang and Dongjiang) are considered as tributaries. At present, the climate in the Pearl River catchment is characterized by a pronounced rainy season in May and June (~300 mm/month), decreasing progressively in July, August, and September (~200–150 mm/month). The precipitation during this warm ($30^{\circ}\text{C} \pm 10^{\circ}\text{C}$) summer season accounts for more than 70% of the annual amount [Wu *et al.*, 2013]. The lowest precipitation rates take place during the colder ($15^{\circ}\text{C} \pm 10^{\circ}\text{C}$) winter months, from November to January (50 mm/month) [Liu *et al.*, 2007 and references therein]. Most part of the annual detrital discharge occurs during the rainy season and on the annual basis, the Pearl river transports about $350 \times 10^9 \text{ m}^3$ of freshwater and more than 100 millions of tons of sediments [Liu and Stattegger, 2014]. At sea, it gives rise to a mud tongue to the west of its mouth located at about 23°N [Qin, 1963; Owen, 2005; Liu *et al.*, 2014]. The geology of the Pearl River catchment is dominated by Mesozoic and Paleozoic cratonic rocks. Limestones constitute about 32% of the total catchment. They dominate in the western part of the basin while granites and sedimentary rocks (shales, limestones, and sandstones) are present in the eastern part.

The Red River is very restricted along a NW-SE direction, channeled by an active strike-slip fault (called the Red River fault) [Schoenbohm *et al.*, 2006]. Consequently, it flows in a nearly straight line from the Yunnan province (China) to Hanoi, established at the head point of its delta at about 20°N in northern Vietnam (Figure 1b). About 50 km NW of Hanoi, it receives waters from two main tributaries: the Lo River and the Da river flowing southward and northward, respectively (Figure 1b). The delta is made of five branches with the two southernmost ones being presently the main sediment contributors to the SCS [Duc *et al.*, 2007]. The relatively warm and humid season occurs later in the year than in the region of the Pearl River mouth. The rainfalls exceeding 10 cm/month start in May and the maximum (>30 cm/month) is reached in August. The winter-dry months are November–March. The river transports about 130–140 millions of tons of sediment/year [Milliman and Syvitski, 1992] from a drainage area largely dominated by Paleozoic to Mesozoic sedimentary rocks. A few metamorphic and igneous formations are also present.

The third highly important fluvial system we studied is the Mekong River reaching the southern part of the SCS at about 10°N in southern Vietnam (Figure 1c). The catchment basin of the Mekong is very extended, starting in the high eastern Tibetan plateau and crossing or bordering several countries through the Indochinese peninsula down to its main alluvial plain in southern Vietnam. The river extends along a NNW-SSE orientation and undergoes extreme seasonal variations in its flow. The upstream region of the river system is the high eastern Tibetan plateau which undergoes much colder humid season than the delta plain where temperatures are rather uniform all year long. This first part of the river path, down to Yunnan province is narrow and steep, often aligned with the main continental strike-slip faults adjusting the Indian-Asian collision. This path induces a strong flow with active erosion and river incision. This upper basin of the Mekong River contributes to about 20% of the water in the Mekong River and about 50% of the total sediment transported by the river which is about $166 \times 10^6 \text{ tons/yr}$ [Liu and Stattegger, 2014]. The geology of this upper path of the Mekong River is dominated by Paleozoic-Mesozoic carbonates and low-grade metamorphic rocks among which sandstones and shales, and continental red beds covering a Precambrian metamorphic basement. From the southern Yunnan downstream, the river valley gets wider and the flow is slower. This lower basin is mainly made of Quaternary and Cenozoic sandstones and mudstones with several Pliocene to recent volcanic bodies along the left bank [Panagos *et al.*, 2011]. The right bank of the lower Mekong is fed by the main tributary Mun which in turn, receives the waters from the Chi river, both incising the Khorat plateau in NE Thailand, covered by Jurassic and Cretaceous sandstones, siltstones, and clays [Ridd *et al.*, 2011]. The path of the Mekong River changed through geological times due to the uplift of the Tibetan plateau. Since mid-Holocene, following the connection between the Mekong and Tonle Sap lake system from Cambodia [Penny, 2006], very large amounts of sediments accumulated at the mouth of the river and the delta prograded southeastward by 200 km [Nguyen *et al.*, 2000].

Seasonal variations in water and sediment loads, geochemistry, sedimentology, and clay composition of the suspended sediments or surface sediments from the estuaries or from the river banks of the three rivers have been studied [Zhang and Wang, 2001; Zhou *et al.*, 2004; Xia *et al.*, 2004; Liu *et al.*, 2007; Zhang *et al.*, 2008, 2012; Liu *et al.*, 2014]. Clay mineralogy and major element content combined with Rb, Sr, Nd concentrations, and Sr-Nd isotopic data indicate that the Pearl River basin undergoes a much higher degree of hydrolysis than the two other rivers, leading to a stronger chemical weathering intensity [Liu *et al.*, 2007, 2016]. In the Red River and the Mekong River, in addition to the weathering process related to the monsoon

climate, tectonic activity/uplift giving rise to strong river incision results in an intense physical erosion of the bedrocks [Liu *et al.*, 2007]. Liu *et al.* [2007, 2016] showed that, although the geology is variable in each catchment, the clay fraction is rather uniform at the basin-scale. Also, because all the three region experience similar humid seasons (although variable in latitudes) the differences in clay mineralogical composition observed from one basin to another are attributed by these authors to variable chemical weathering versus physical erosion intensities.

3. Samples and Methods

The sampling has been conducted both in the main streams and in the tributaries of the three rivers [Liu *et al.*, 2007, 2016]. About 2 kg of sediment were collected per site in a 1–2 cm thick layer either from river beaches near the water-level or from the river bed at water depths lower than 1 m [Liu *et al.*, 2007]. The sampling sites were selected to avoid contamination from riverbank sediments and potential manmade pollution. Fieldworks were carried out during the dry seasons (January–March) so that the collected samples illustrate fresh suspended sediments deposited during the previous humid season. The sediment was kept at $\sim 4^{\circ}\text{C}$.

The small fraction dedicated to the magnetic analyses was separated into different specimens for the different laboratory analyses performed at LSCE (Gif-sur-Yvette, France) and IGG-CAS (Beijing, China) to characterize the magnetic mineralogy, grain size, and relative contributions of the different magnetic minerals to the bulk magnetic signal of the collected sediments. The magnetic properties have been analyzed in 18 samples from the Pearl River system, 21 samples from the Red River, and 17 samples from the Mekong River delta. The distribution of the samples along the three rivers, their tributaries, and their delta is given in Figure 1.

Plastic cubes ($2 \times 2 \times 2$ cm) filled up with humid sediment were used for the low-field magnetic susceptibility which was measured at two different frequencies (low: 0.465 kHz, high: 4.65 kHz) with an MS2B Bartington sensor at LSCE. The measurements were made over a 10 s integration time. The measurements were repeated 5–10 times for each sample and each frequency. The frequency dependence $\chi_{fd}(\%)$ has been calculated using $\chi_{fd}(\%) = (\overline{\chi_{lf}} - \overline{\chi_{hf}}) \times 100 / \overline{\chi_{lf}}$ where $\overline{\chi_{lf}}$ and $\overline{\chi_{hf}}$ are the average values of the 5–10 data obtained at low and high frequencies, respectively.

An anhysteretic remanent magnetization (ARM) was imparted to the same cubes using a 50 μT DC field superimposed to a 100 mT alternating field (AF). The susceptibility of ARM (χ_{ARM}) was calculated from this value. This ARM was then stepwise demagnetized up to 80 mT using 10 successive steps (5, 10, 15, 20, 25, 30, 35, 40, 60, 80 mT) using an AGICO LDA-3A-demagnetizer. The magnetization decreased regularly through the demagnetization allowing to calculate the median destructive field of ARM (MDF_{ARM}) and the percentage of magnetization remaining after demagnetization at 80 mT with respect to the initial value ($ARM_{80\text{ mT}}\% = 100 \times ARM_{80\text{ mT}} / ARM_{0\text{ mT}}$).

The isothermal remanent magnetization (IRM) was then stepwise acquired on the same cubes with six successive steps up to 1 T using an Applied Physics pulse magnetizer. This $IRM_{1\text{ T}}$ was then stepwise AF demagnetized using the same steps as for the ARM. In the same way as for ARM, MDF_{IRM} and $IRM_{80\text{ mT}}\%$ have been calculated. The S-ratio was calculated after applying a 0.3T backfield to the $IRM_{1\text{ T}}$. We used the original definition of the S-ratio $= (-IRM_{-0.3\text{ T}} / IRM_{1\text{ T}})$ [King and Channell, 1991].

The hysteresis loops were performed using an AGM (Micromag 2900) between +1 and -1 T on smaller dry specimens weighting 4–6 mg. As these chips are small, multisamples analyses conducted on randomly selected sites allowed us to check their representativeness. Saturation magnetization (M_s), remanent saturation magnetization (M_{rs}), and coercive force (H_c) were determined after high field slope correction. The remanent coercive force (H_{cr}) was determined by applying increasing back-fields after saturation at 1 T. To quantify the contribution of the different coercivity families to the total IRM, high-resolution IRM acquisition curves (120–200 data points between 0 and 1 T in a log distribution of the field steps) were decomposed into cumulative log Gaussian (CLG) curves [Robertson and France, 1994] using the software proposed by Kruiver *et al.* [2001]. The different coercivity families are defined by their half saturation IRM (SIRM) field ($B_{1/2}$) and the percentage of their contribution to the total IRM.

The first-order reversal curves (FORCs) were measured with a vibrating sample magnetometer (Princeton Measurements Corporation VSM3900) according to the protocol described by Roberts *et al.* [2000] and Egli *et al.* [2010]. A total of 100–450 FORCs were measured with a positive saturation field of 1.0–2.0 T, increasing field steps (δH) of 1.7–0.5 mT, and an averaging time of 200–400 ms, depending on the magnetic mineralogy and concentration. The FORC diagrams were calculated using the FORCinel version 2.05 software [Harrison and Feinberg, 2008] with smoothing factor of 3 or 6 depending on the samples and FORC resolution.

In order to have access to the thermal behavior of the samples, we conducted high-temperature demagnetization of three-axes IRM on at least two cubic specimens (8 cm^3) per river system, selected on the basis of the previous measurements. The cubes were dried and fields of 1, 0.3, and 0.1 T were successively applied to their three different axes using the Applied Physics pulse magnetizer. The samples were then demagnetized between room temperature and 700°C , using a zero-field PYROX furnace in which the temperature is controlled by three independent heating cells, keeping the temperature gradient lower than $3\text{--}4^\circ\text{C}$ at high temperature over the interval in which the samples are placed.

All remanent magnetizations (IRM, ARM, three-axes IRM) were measured using a 2G-755R cryogenic magnetometer equipped with high-homogeneity pick-up coils and placed together with the zero-field furnace within the μ metal shielded room at LSCE.

Low-temperature magnetic measurements were performed with a Quantum Design Magnetic Property Measurement System (MPMS XP-5, sensitivity = $5.0 \times 10^{-10} \text{ Am}^2$). Zero-field-cooled (ZFC) and field-cooled (FC) curves were obtained by cooling samples from 300 to 10 K in zero field and in a 2.5 T field, respectively, followed by imparting a SIRM in a 2.5 T field (hereafter termed as SIRM_{10K_2.5T}), and then measuring the remanence in zero field during warming to 300 K. Low-temperature cycling (LTC) of a SIRM acquired at a 2.5 T field at 300 K (hereafter termed SIRM_{300K_2.5T}), was measured in zero field during a cooling-warming cycling (300→10→300 K).

4. Results

4.1. Pearl River

The magnetic parameters are variable depending on the location of the sampling sites along the river and along the tributaries (supporting information Table S1 and Figure 1).

The bulk magnetic parameters largely vary by a factor of 15 for χ_{ARM} , 30 for χ_{IF} and 50 for IRM_{1 T} (supporting information Table S1, Figures 2a–2c). This variability may be due to changes in concentration of magnetic grains and also to changes in magnetic mineralogy and grain size. It is therefore important to determine the nature of the magnetic minerals. The majority of the samples are characterized by high S-ratio (≥ 0.95 ; Figure 2d), low H_c and H_{cr} (average around 13 and 38 mT, respectively, Figure 2e), low MDF_{ARM} and MDF_{IRM} (average around 15 mT; Figure 2h), and low $\text{ARM}_{80 \text{ mT}\%}$ and $\text{IRM}_{80 \text{ mT}\%}$ ($<2\%$ and 7% , respectively; Figure 2g). They therefore contain a dominant part of low-coercivity magnetic grains. In the samples where S-ratio is lower than 0.95, $\text{IRM}_{80 \text{ mT}\%}$, MDF_{IRM} , H_c , and H_{cr} increase with decreasing S-ratio. MDF_{ARM} and $\text{ARM}_{80 \text{ mT}\%}$ slightly increase (Figure 2, supporting information Table S1). These samples therefore contain significant amounts of higher coercivity fraction. Changes in the relative proportion of high/low-coercivity minerals is illustrated by the shape of the IRM acquisition curves (Figure 3a) and by hysteresis curves being progressively more wasp-waisted when the S-ratio decreases (PR13 compared to PR18 in Figure 3c).

The IRM acquisition curves could be decomposed into four CLG curves. The first two have $B_{1/2}$ of about 2 and 7 mT, respectively, and represent less than 5% and between 5 and 19% of the total IRM, respectively. The dominant fractions are those corresponding to $B_{1/2}$ between 25 and 55 mT (42 mT average) and $B_{1/2}$ between 200 and 630 mT (average 545 mT) (labeled CLG#3 and CLG#4, respectively, in Figure 3b). The contribution of CLG #3 and #4 are inversely correlated: CLG #3 decreases from $\sim 84\%$ to $\sim 20\%$ when CLG #4 increases from $\sim 3\%$ to $\sim 75\%$ (Figures 2f and 3b). The FORC diagrams confirm that the coercivity spectrum change depending on the samples (e.g., PR13 compared to PR18, Figure 3d).

The thermal behavior of the two coercivity families have been examined by thermal demagnetization of three-axes IRM of two samples: PR17 representing the samples in which low-coercivity fraction is dominant and PR37 representing the samples in which high coercivity is significantly contributing to the magnetic signal (Figure 3e). It is typical for magnetite with a removal of all components between 550°C and 600°C . An

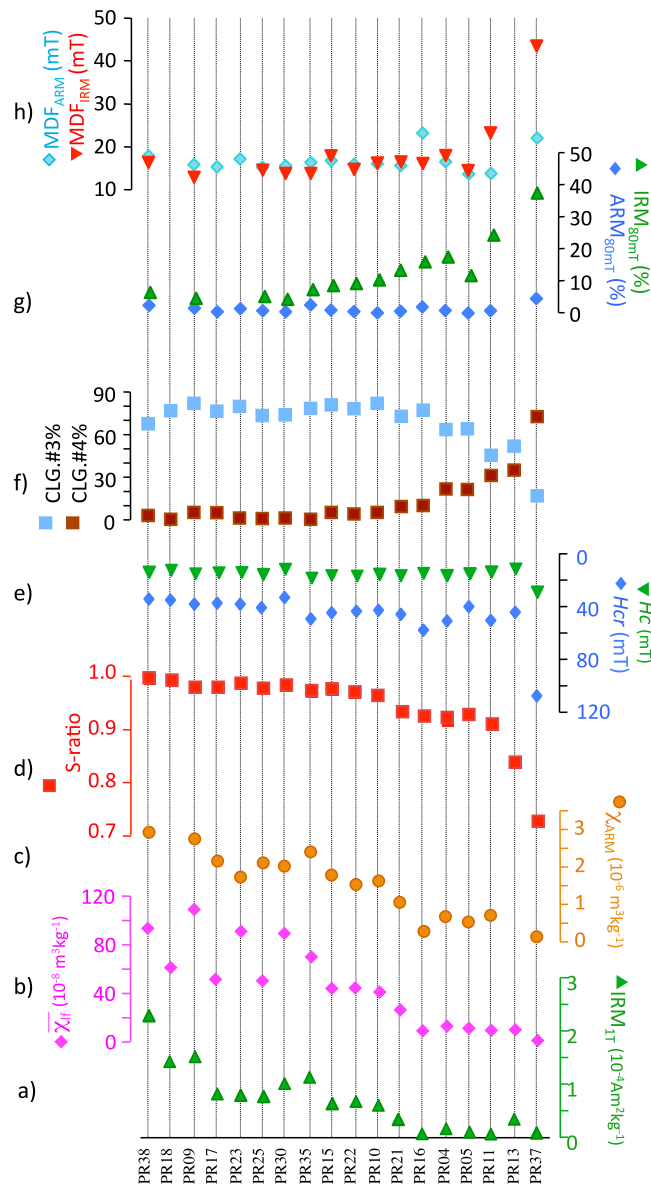


Figure 2. Magnetic parameters obtained from the Pearl River organized from left to right by decreasing S-ratio (d). IRM_{1T} (a) is the isothermal remanent magnetization acquired at 1 T, $\bar{\chi}_{lf}$ (b) is the average value of the 5–10 measurements of the low-field (low-frequency) magnetic susceptibility. χ_{ARM} (c) is the susceptibility of the anhysteretic remanent magnetization. H_{cr} and H_c (e) are the remanent coercitive field and the coercitive field, respectively. CLG#3 and #4 (f) are the two main components identified by decomposing the IRM acquisition curve into cumulative log Gaussian curves. CLG#3 and #4 illustrate the contribution of low-coercivity and high-coercivity components, respectively, to the IRM_{1T} . $ARM_{80\text{ mT}}$ (%) and $IRM_{80\text{ mT}}$ (%) (g) are the percentages of the remaining ARM and IRM intensities after demagnetizing them to 80 mT. Finally, MDF_{ARM} and MDF_{IRM} (h) are the median destructive field of ARM and IRM.

For example for the first three sites reported in Figure 4 (RS06, 11, 12), the bulk parameters vary by a factor of 2–3 while the S-ratio uniformly exceeds 0.95. The samples therefore contain variable magnetic concentrations and also different types of magnetic minerals.

For all sites but RS41 and RS01, the S-ratio is distributed between 0.96 and 0.83 (Figure 4d, supporting information Table S1). This decrease is accompanied by a general increase of $IRM_{80\text{ mT}}$ from about 7% to about 23% (Figure 4d, supporting information Table S1). H_{cr} also increases from about 30 mT to about 80 mT

inflexion in the low-coercivity curves around 300°C may also indicate some small participation of sulphides. The high-coercivity magnetic carrier, when present, is hematite as indicated by the complete removal of the magnetization between 650°C and 690°C (PR37 in Figure 3e). The low-temperature experiments confirm the presence of magnetite with the Verwey transition clearly visible (LTC cycles, Figure 3f). Hematite is difficult to identify at low temperature in particular when magnetite is dominant but in the samples where hematite is more abundant, the amplitude of the intensity change at the Verwey transition is smaller than in the other samples (PR13 in Figure 3f).

When the hysteresis parameters obtained only from samples containing mainly magnetites (CLG #4 <10% and S-ratio ≥ 0.9) are plotted on a Day diagram [Day et al., 1977], it appears that this fraction is within the pseudo-single domain range (Figure 3d). In that coercivity family, the FORC diagrams also indicate the presence of interacting single domains, consistently with relatively high χ_{fd} reaching 8% (supporting information Table S1).

The magnetic signal of the samples from the Pearl River is therefore mainly carried by single domain and pseudo-single domain magnetites with locally some hematite contribution.

4.2. Red River

In the Red River, except for two sites (RS41 and RS01), the three bulk parameters IRM_{1T} , χ_{lf} , and χ_{ARM} , varying by a factor of 6, 4, and 5, respectively, are more uniform than in the Pearl River (Figures 4a–4c, supporting information Table S1). This small variability does not necessarily find its counterpart in the other parameters reported in Fig-

ure 4. For example for the first three sites reported in Figure 4 (RS06, 11, 12), the bulk parameters vary by a factor of 2–3 while the S-ratio uniformly exceeds 0.95. The samples therefore contain variable magnetic concentrations and also different types of magnetic minerals.

For all sites but RS41 and RS01, the S-ratio is distributed between 0.96 and 0.83 (Figure 4d, supporting information Table S1). This decrease is accompanied by a general increase of $IRM_{80\text{ mT}}$ from about 7% to about 23% (Figure 4d, supporting information Table S1). H_{cr} also increases from about 30 mT to about 80 mT

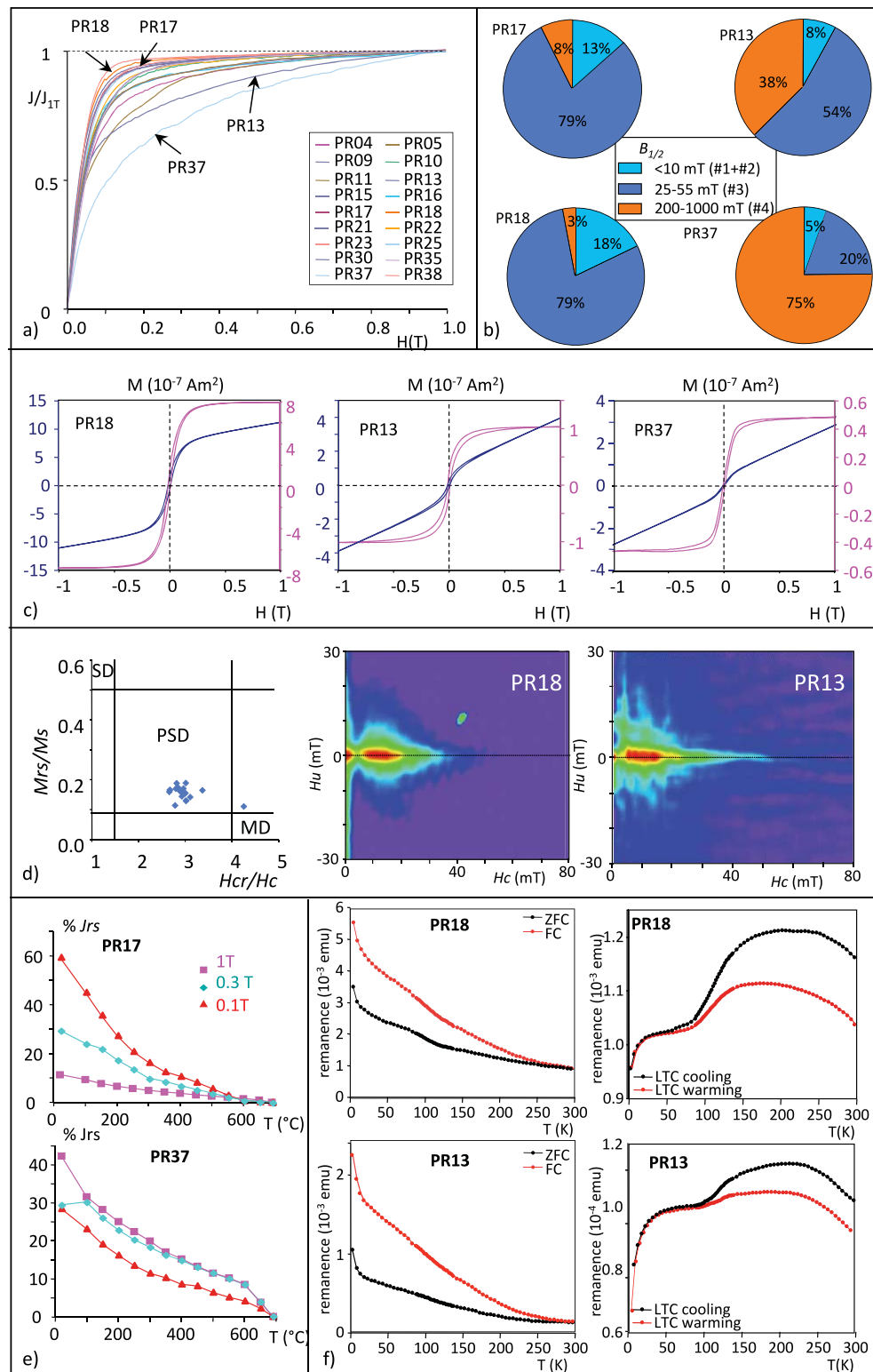


Figure 3. Results of magnetic analyses obtained from representative samples from the Pearl River: (a) stepwise IRM acquisition curves where the curves corresponding to the further analyzed samples are identified; (b) relative contribution of the different CLG component to the total IRM for the selected samples; (c) hysteresis curves (in blue before and in pink after correction for the paramagnetic component); (d) Day diagram (SD: single domain; PSD: pseudo-single domain; MD: multidomain) and FORC diagrams (120 FORCs were measured with a positive saturation field of 1 T, a field increment (δH) of 1.61 mT, and an average time of 400 ms, and calculated with a smooth factor of 3); (e) results of the thermal demagnetization of three-axes IRM; and (f) low-temperature spectra (see text).

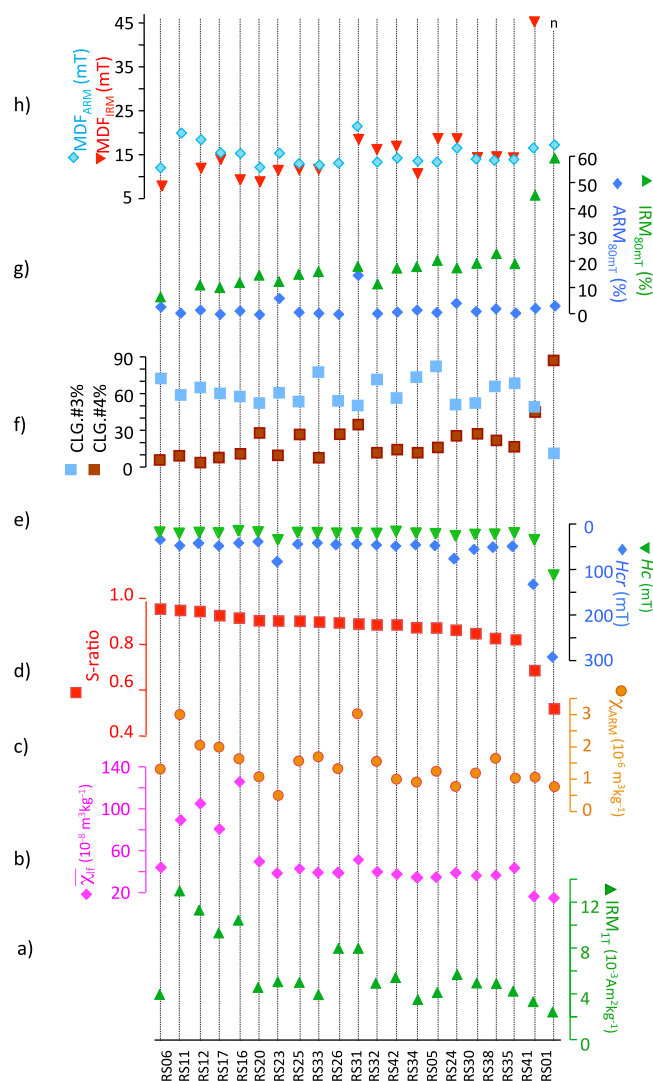


Figure 4. Magnetic parameters obtained from the Red River organized from left to right by decreasing S-ratio. See Figure 2 for the explanation about the different parameters. In (h), n is for the samples for which MDF_{IRM} could not be determined because it exceeds 80 mT (see text).

The hysteresis curves of the samples characterized by lower S-ratio indeed show a higher saturation field (RS26 compared to RS11 in Figure 5c). The three-axes IRM thermal demagnetization indicates that the high-coercivity component they contain is hematite (1T component of RS26 removed between 650 and 690°C; Figure 5e). The thermal spectra of the other samples (see RS11 in Figure 5e) indicate the presence of magnetites with coercivities lower than 0.3 T and sulphides (most likely greigite) for the axis corresponding to coercivities between 0.3 and 1 T (Figure 5e). The Verwey transition is more marked for samples with higher S-ratio (RS12 compared to RS34) but it remains very clear in the higher coercivity samples as well (Figure 5f). Small amounts of hematite are also reported by *Nguyen et al.* [2016] along the main stream although these authors did not observe it at all their sites. This may be due to the fact that the κ -T curves they used may not be the most sensitive method. For example no hematite is observed in the κ -T curve at their site ND2 while high-coercivity fraction is clearly identified from the IRM gradient curve from the same site.

The hysteresis parameters of the samples characterized by the lowest coercivity (S-ratio ≥ 0.9) indicate that the magnetite grains are in the pseudo-single domain range, slightly coarser than in the Pearl River (Figure 5d) and the FORC diagrams are indeed more toward multidomain type (Figure 5d). However, it is difficult to estimate magnetic grain size, even using physical methods giving access to the domain state such as the hysteresis curves because this is mainly known for magnetite. The results might therefore be biased by the

(Figure 4e, supporting information Table S1). The MDF_{ARM} and MDF_{IRM} are variable without showing any trend. Obviously, all these samples contain low-coercivity minerals mixed with variable amounts of higher coercivity fraction. This is also illustrated by slightly variable shapes of IRM acquisition curves, not entirely reaching the saturation state at 1T (Figure 5a). The decomposition of the IRM acquisition curves into CLG allows to identify four components with $B_{1/2}$ around 5, 13, 51, and 580 mT, similar to the Pearl River. As in the Pearl River as well, the first two families have a minor contribution to the total IRM (about 8% and 7%, respectively, as an average) (Figure 5b). Therefore the two other components (labeled again CLG #3 and #4) are inversely correlated (Figure 4f). The CLG#3 is contributing less than in the Pearl River ($\sim 64\%$ compared to $\sim 75\%$) while CLG #4 contributes more ($\sim 17\%$ compared to $\sim 12\%$). The relative contribution of these two components, does not always vary consistently with the S-ratio. For example, RS20, RS25, RS26, and RS31 are characterized by higher contribution of CLG #4 than other sites having about the same S-ratio. It indicates that this coercivity fraction is most likely made of a mixture of largely overlapping spectra. The hysteresis curves of the samples characterized by lower S-ratio indeed show a higher saturation field (RS26 compared to RS11 in Figure 5c). The three-axes IRM thermal demagnetiza-

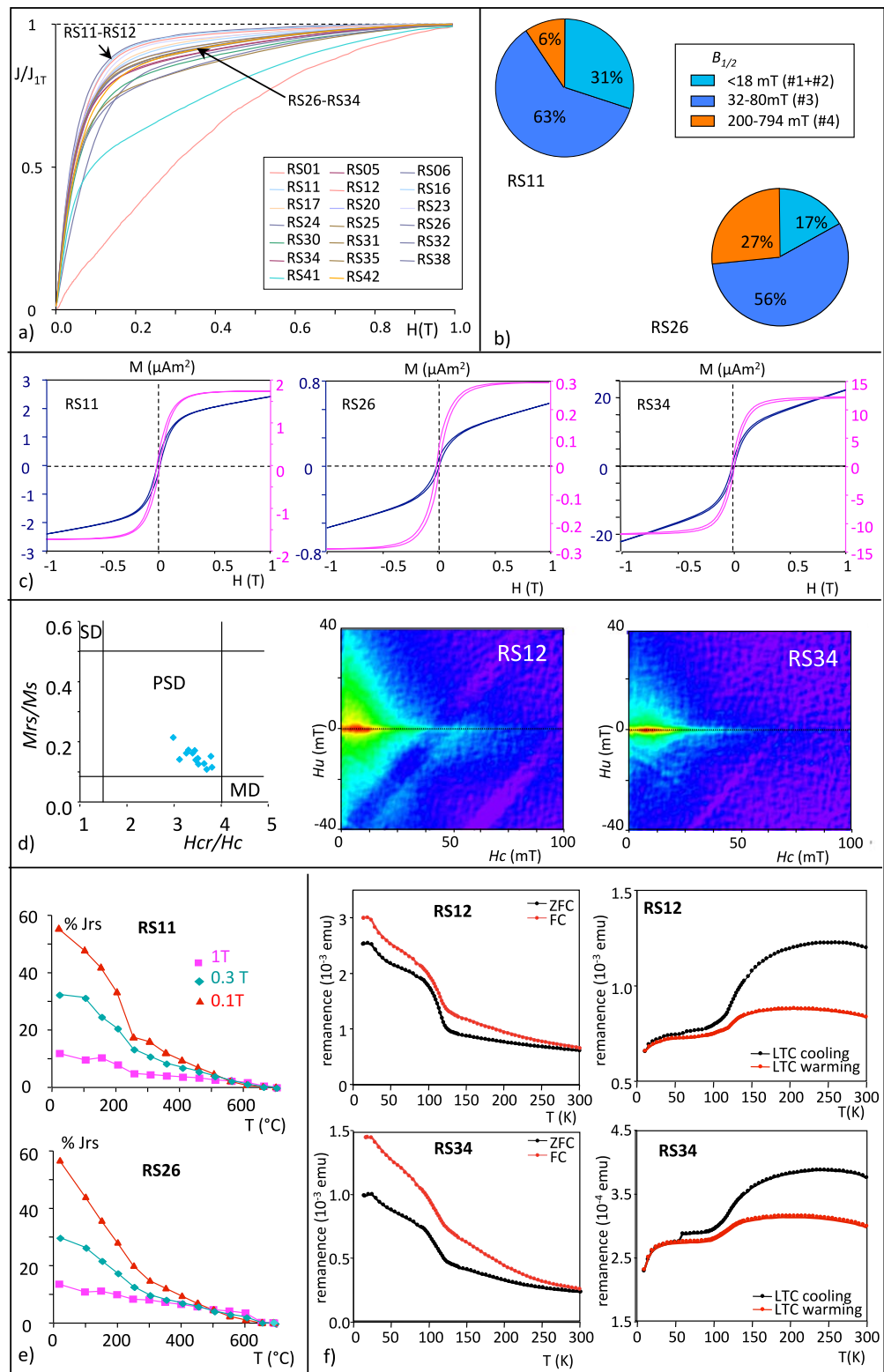


Figure 5. Results of magnetic analyses obtained from representative samples from the Red River (same as for the Pearl River in Figure 3). For both RS12 and RS34, 350 FORCs were measured with a positive saturation field of 1 T, a field increment (δH) of 0.534 mT, and an average time of 400 ms, and calculated with a smoothing factor of 6.

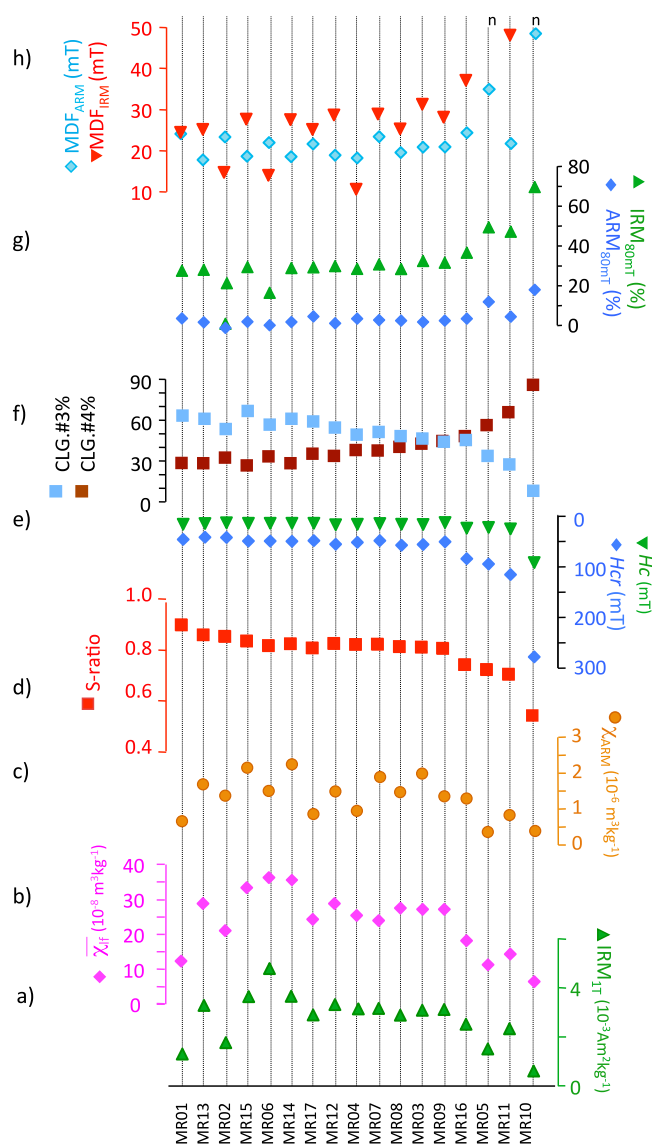


Figure 6. Magnetic parameters obtained from the Mekong River organized from left to right by decreasing S-ratio. See Figure 2 for the explanation about the different parameters. In (h), n is for the samples for which MDF_{IRM} could not be determined because it exceeds 80 mT (see text).

The three bulk parameters (IRM_{T} , χ_{if} , and χ_{ARM}) largely covary in the Mekong River (Figures 6a–6c; supporting information Table S1). The S-ratio is everywhere lower than 0.9 with values reaching 0.54 (site MR10) (Figure 6d). The other parameters consistently show high-coercivity contributions with H_{cr} between 40 and 276 mT (average 71 mT), H_c between 12 and 91 mT (average 20 mT), $IRM_{80\text{ mT}}$ (%) between 16 and 70% (average 34%) and MDF_{ARM} between 18 and 49 mT (average 23 mT) (Figures 6e–6h, supporting information Table S1). MDF_{IRM} could not be defined for two samples because it exceeds 80 mT (i.e., the last peak field used for the AF demagnetization ($IRM_{80\text{ mT}}\% > 50\%$)) (Figures 6g, 6h; supporting information Table S1). This high content in high-coercivity minerals is also illustrated by the IRM acquisition curves, all far from reaching the saturation state (Figure 7a). Lower is the S-ratio, more wasp-waisted are the hysteresis curves and more significant is the contribution of the CLG #4 ($B_{1/2}$ between 400 and 800 mT) which reaches 87% of the total IRM at site MR10 (Figures 7b, 7c; supporting information Table S1).

The FORC diagrams were performed over a progressively larger H_c range when S-ratio decreased. The three diagrams shown in Figure 7d are constructed with curves acquired at maximum H_c fixed at 40 mT (MR02),

hematite content. *Nguyen et al.* [2016] investigated the magnetic grain-size variations in the Red River using empirical ratios χ_{ARM}/χ and $\chi_{ARM}/SIRM$ yielding information about relative changes in magnetite grain size. They also concluded about some degree of variability in the coarse range. The observed variability is most likely due to changes in the mineralogical composition and/or to the spatial and/or time differences in local hydrodynamics of the river (higher turbulences may occur in some meanders).

The two sites RS41 and RS01 have magnetic properties very different from the other studied sediments from this river system. They are characterized by S-ratio lower than 0.7 (Figure 4d), high H_{cr} (130 and 290 mT, respectively) and H_c (27 and 104 mT, respectively) (Figure 4e), dominant CLG #4 ($> 40\%$; Figure 4f), $IRM_{80\text{ mT}}\% > 45\%$ (Figure 4g) and high MDF_{IRM} (46 mT for RS 41 and not defined because > 80 mT for RS01; Fig 4h). They are obviously dominated by high-coercivity fraction, most likely by hematite as in the other sites.

In summary, the magnetic signal of the Red River samples is dominated by pseudo-single/multidomain magnetites. Given the much lower intensity of hematite compared to magnetite, the observed coercivity distribution argues for rather significant amounts of hematite sometimes accompanied by small amounts of greigite.

4.3. Mekong River

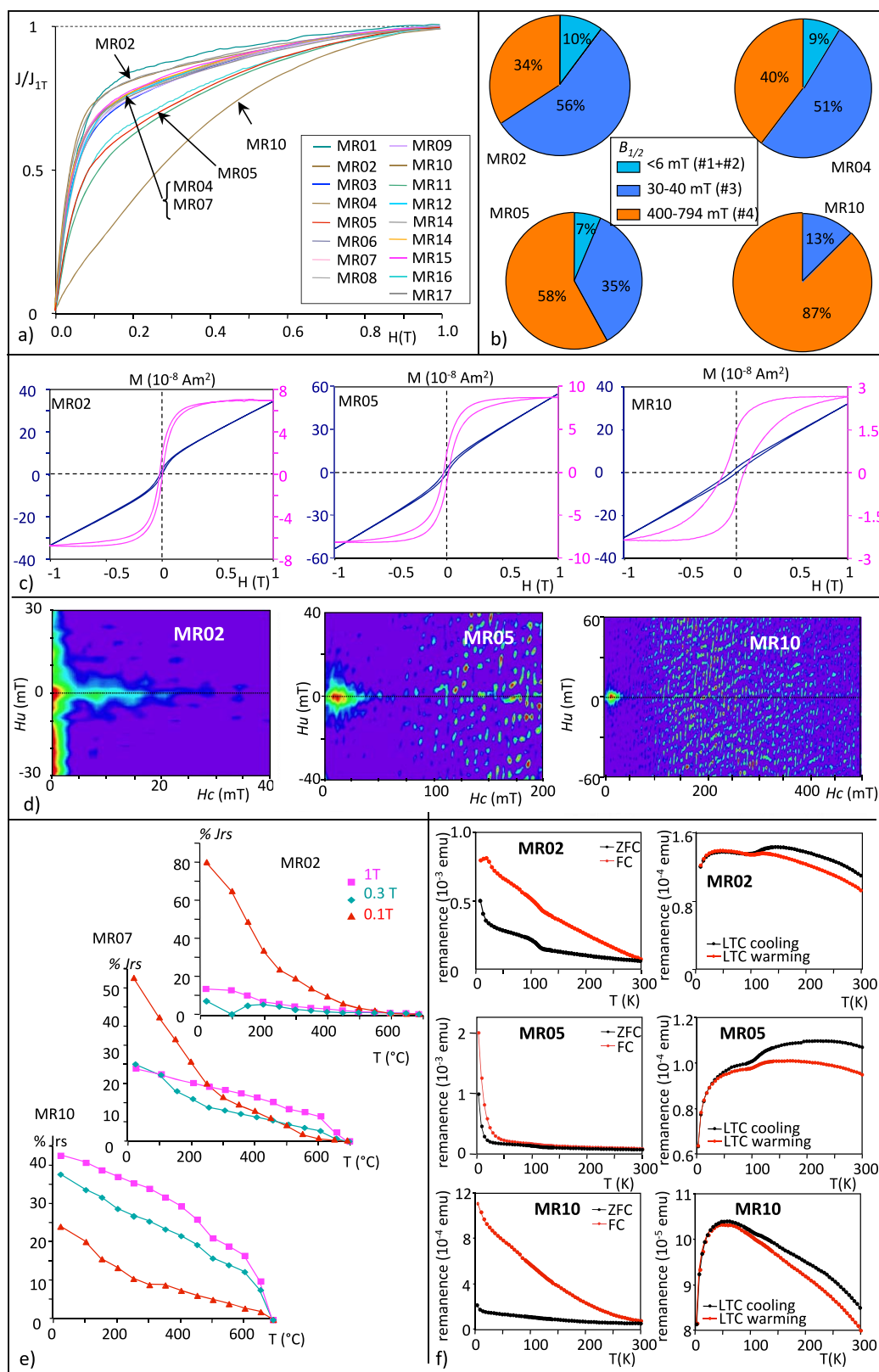


Figure 7. Results of magnetic analyses obtained from representative samples from the Mekong River (same as for the Pearl River in Figure 3). For MR02, 100 FORCs were measured with a positive saturation field of 1 T, a field increment (δH) of 1.61 mT, and an average time of 200 ms, and calculated with a smoothing factor of 3. For MR05, 180 FORCs were measured with a positive saturation field of 2 T, a field increment (δH) of 1.68 mT, and an average time of 400 ms, and calculated with a smooth factor of 3. For MR10, 420 FORCs were measured with a positive saturation field of 2 T, a field increment (δH) of 1.52 mT, and an average time of 300 ms, and calculated with a smooth factor of 3.

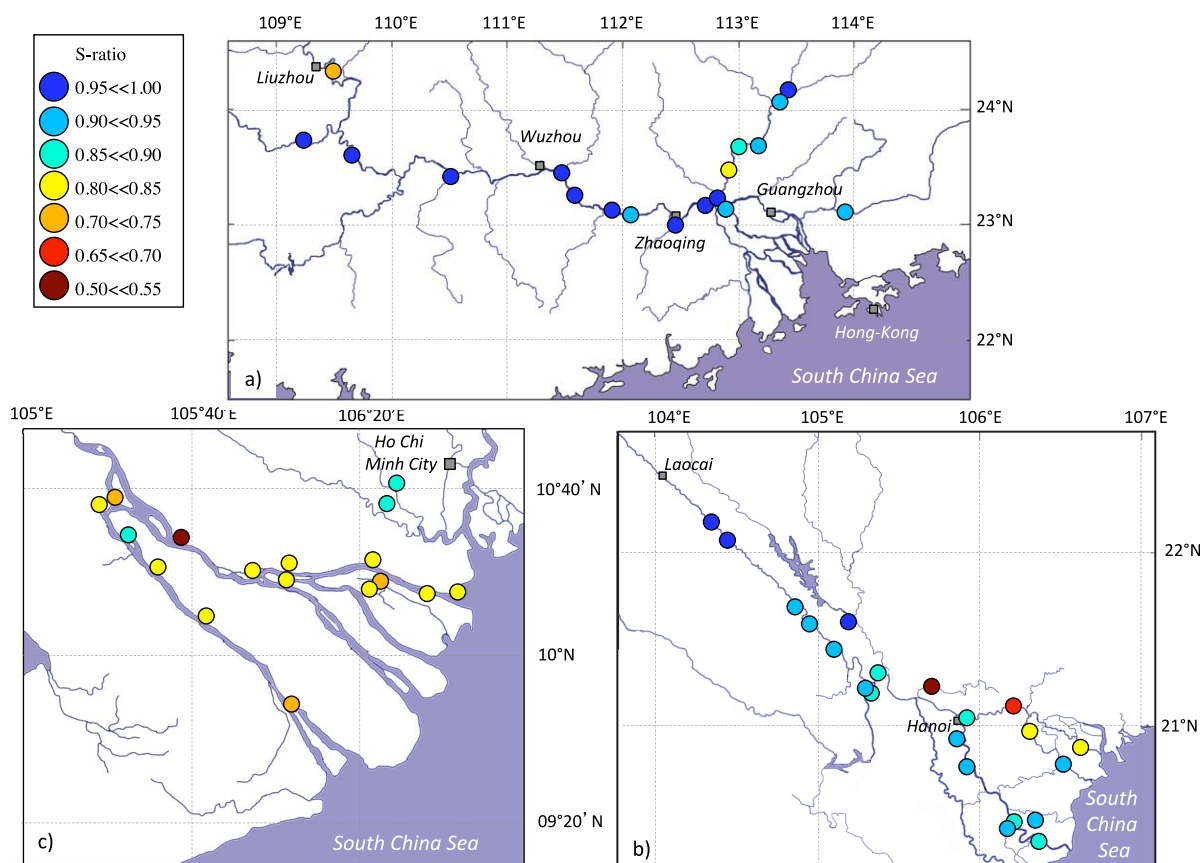


Figure 8. Geographical distribution of the magnetic properties (illustrated as the S-ratio) in each river: (a) Pearl River; (b) Red River; and (c) Mekong River.

200 mT (MR05), and 500 mT (MR10). MR02 which represents the group of samples with the highest S-ratio is characterized by low-coercivity multidomains. The other two samples shown in Figure 7d (MR05: S-ratio = 0.72 and MR10: S-ratio = 0.54) show interacting single-domain low-coercivity particles mixed with high-coercivity particles and most likely antiferrimagnetic particles illustrated by the colored spots at high field ($H_c > 100$ mT).

The thermal demagnetization of the three-axes IRM is more informative in terms of magnetic carriers. The results are illustrated in Figure 7e with three samples representative of the different types of IRM acquisition curves. The intensity of IRM acquired at 1 and 0.3 T progressively increases from samples MR02 to MR07 and to MR10. This magnetization, removed between 650°C and 700°C, clearly illustrates hematite. The low-coercivity component carried by the 0.1 T axis exhibits a first decrease between room temperature and about 300°C followed by a slower decrease up to the full demagnetization around 600°C (except in MR10 where it resists up to ~700°C). The presence of magnetite in these samples is also observed with the clear Verwey transition (Figure 7f). This transition is not seen in MR10 where magnetite is very minor (Figure 7f). The significant abrupt drop of intensity below 20 K is most likely due to antiferrimagnetic particles.

This set of experiments indicates that the sediment in the Mekong River is dominated by hematite with small or no amount of magnetites (and sometimes, most probably sulphides).

5. Discussion

In the three river systems, the variability in the magnetic content mainly consists in changes in the relative contribution to the total magnetization of low and high-coercivity families identified as corresponding to magnetites (and sometimes a minor contribution of sulphides) and hematites, respectively. Goethite, resulting from very high hydrolysis processes is not observed. In Figure 8, the geographical distribution of these

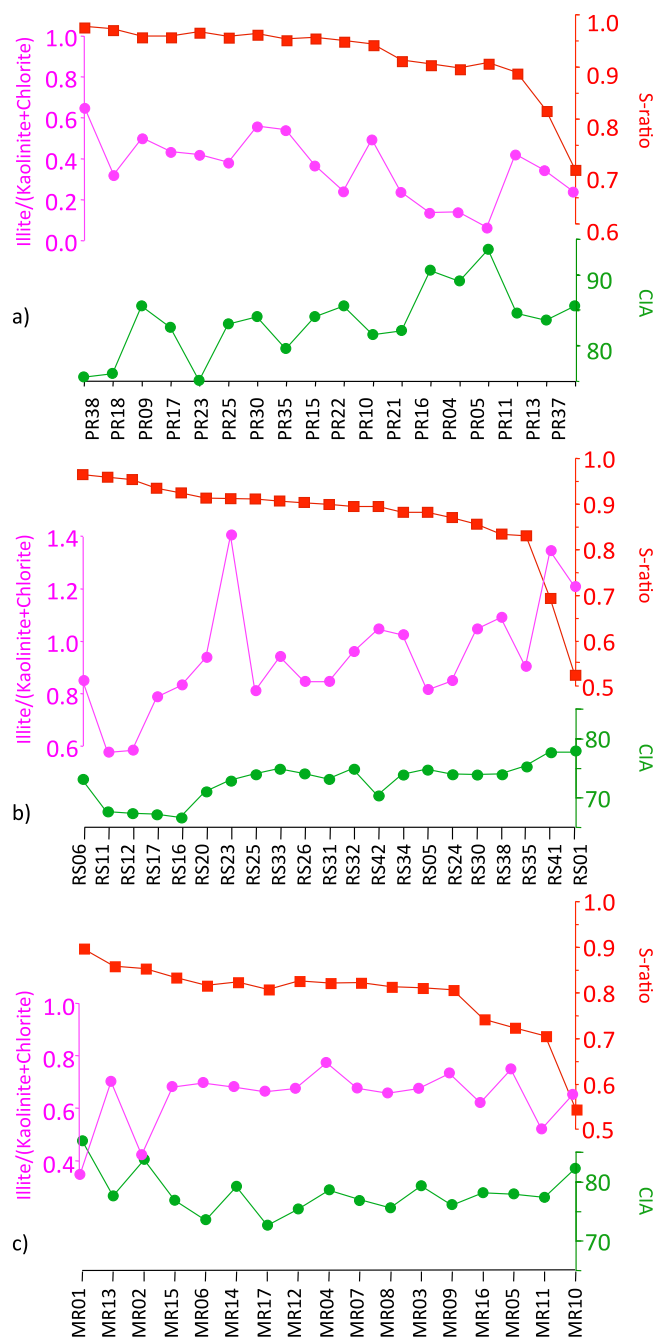


Figure 9. Magnetic properties illustrated by the S-ratio (in red) compared to the clay mineralogy and the chemical index of alteration (CIA) as reported in Liu et al. [2007].

variable mixtures is illustrated by dots, the color of which depends on the S-ratio range. The figure would be exactly the same if we had taken CLG#4, MDF_{IRM} , or $IRM_{80\ mT}(\%)$ instead of S-ratio. Significantly different magnetic properties characterize each basin in which slight internal variations are also observed. The magnetic mineralogy can be compared to the other components of the detrital fraction, in particular the clay mineralogy and the major element content [Liu et al., 2007]. In the clay fraction, the main duality is between illite and kaolinite, the first illustrating more physical erosion than the second, more sensitive to chemical weathering. The percentage of smectite slightly increases from the Pearl River to the Red River and to the Mekong River where, however, it remains a minor component (11% as an average) [Liu et al., 2007]. The relative concentrations of clay minerals expressed as the ratio illite/(kaolinite + chlorite) increases (decreases) with the increasing (decreasing) contribution of erosion versus weathering. This ratio is plotted in Figure 9 as a function of increasing magnetic coercivity illustrated by the S-ratio. Out of the major element content, the chemical index of alteration (CIA = molar ratio of $[Al_2O_3 = (Al_2O_3 + CaO + Na_2O + K_2O)] \times 100$) [Nesbitt and Young, 1982] calculated at each site [Liu et al., 2007] is also compared to the main magnetic properties (Figure 9).

In the Pearl River basin, the main stream is richer in magnetites than the northern and eastern branches (Figure 8a). The highest proportion of hematite is found at site PR37, along a tributary in the westernmost part of the studied area (close to Liuzhou). When

this river reaches the main stream, its hematite contribution is diluted as no significant increase in coercivity is observed at site PR35. The main stream contributing the most to the detrital discharge into the SCS remains therefore rich in magnetites until it meets the northern and eastern branches. The last two have higher concentrations in hematite although the magnetic signal of the two northernmost sites in the northern river (PR09 and PR10) is also dominated by magnetites. No sulphides (greigite) are found in these sediments in contrast with sedimentary cores located off the Pearl River delta and in the sedimentary tongue along the coast [Ouyang et al., 2013]. The latter may have therefore suffered from some degree of diagenesis in the presence of organic matter, obviously not affecting the river sediments.

Kaolinite is the dominant clay fraction in the Pearl River sites and, together with a high illite chemical index (>0.5) and a high illite crystallinity (>0.24), it indicates strong hydrolysis conditions [Liu *et al.*, 2007]. A slight decreasing trend is observed in the illite/(kaolinite + chlorite) content together with the coercivity increase from site PR38 to site PR05 (Figure 9a). The alkalinity index CIA is high and it increases from about 70% to about 88% when magnetic coercivity increases (Figure 9a). All these results are consistently indicating an increasing weathering process with increasing hematite contribution indicating that the latter results from the alteration of parent rocks in the Pearl River basin. Surprisingly, at the three sites (PR11, PR13, and PR37) showing the highest coercivities, illite is slightly more abundant with respect to kaolinite and chlorite and the CIA is lower. This suggests that hematites at these sites do not only result from a higher degree of weathering but also, most likely, from the physical degradation of the local bedrocks.

Finally, the fact that magnetite remains the dominant magnetic carrier along the main stream, indicates that magnetite resists quite well to the weathering processes indicated by the high kaolinite content. The weathering may have eventually increased a little the average size of the magnetite grains which, however, remain in the (pseudo)single domain range.

In the Red River catchment, the magnetite contribution is slightly lower than in the Pearl River. It means that non-negligible amounts of hematites are present although they contribute only for about 20–30% to the total signal, due to the weak magnetization of this oxide. Magnetite therefore remains the dominant carrier of the magnetization in the main stream. Significantly higher contributions of hematite to the total magnetic signal are found in the northern branch of the delta and in the small tributary, north of Hanoi (Figure 8b), illustrating significantly large proportions of hematite in the magnetic fraction. In the Red River catchment, by contrast to the Pearl River, illite dominates the clay fraction. In the studied sites, the illite percentage increases from about 30% up to 55% giving rise to an increase in the illite/(kaolinite + chlorite) ratio along with the increase in the magnetic coercivity (Figure 9b). It is a general trend with no particular distinct signature for the sites located in the northern part of the delta and showing the highest coercivities (Figures 8b and 9b). The CIA is less variable than in the Pearl River (67%–77%) but it similarly increases with the magnetic coercivity (Figure 9b). The chemical and clay analyses conducted in the Red River samples by Liu *et al.* [2007] indicate that the sediments transported by this river mainly originate from physical erosion related to the tectonic incision of the river and probably more active during raining season when the flow is strong. The magnetic mineralogy also suggests some variable degree of weathering depending on the location along the river. The hematite-rich soils developed in the Red River catchment, as illustrated by the color of the river waters, are most likely the main contributors of these high-coercivity hematite particles into the magnetic assemblage.

In the Mekong River, hematite is present everywhere. Its signature is very clear in the magnetic parameters and given the fact that the magnetization of hematite is considerably weaker than that of magnetite [Dunlop and Özdemir, 1997], the values obtained for the different parameters indicate that it is present in large amounts. No downstream trend is observed in the relative contribution of hematite. Site MR13, one of the most upstream site in the studied area is slightly richer in magnetite as well as two sites located in two other river branches in the northern part of the delta (Figure 8c). These northern rivers have tributaries draining the region where Pliocene to recent basaltic lavas are present and that may explain the higher content in magnetites. Given the fact that a large part of the detrital load of the Mekong River originates from the active erosion and incision in the upper part of the catchment [Liu *et al.*, 2007], the hematites may originate from the hematite-rich geological formations cropping out in these regions (Devonian red sandstones and/or Mesozoic continental red beds). Another possible source would be a significant chemical weathering of the original material into hematite in the floodplains where, indeed, lateritic soils are present [Panagos *et al.*, 2011]. However, the clay mineral study suggests that erosion is the main source of illite which dominates the clay fraction in the river [Liu *et al.*, 2007] (Figure 9c). Hematites have most likely the same origin. No changes are observed in the chemistry while the magnetic mineralogy changes. For example, no changes in the clay assemblage and in the CIA are observed at site MR10 compared to the other sites, although it is characterized by a very high contribution (87%) of hematite. This suggests again that the magnetic mineralogy illustrates a different sensitivity to the erosion/weathering balance.

Besides the small variations observed in each catchment, differences are obvious in the composition of the magnetic fraction from one basin to the other (Figure 8). The Pearl River is a magnetite-rich river system and the Mekong River is a hematite-rich system. The sediments from the Red River contain significant

amounts of hematite but their bulk magnetic signal remains dominated by magnetites slightly coarser than in the Pearl River.

6. Conclusive Remarks

The magnetic mineralogy reflects the geology and the hydrology in the catchment of the three studied rivers although we cannot exclude that part of the magnetites might also be of anthropic origin because the floodplains are highly populated, urbanized, and industrialized [Franke *et al.*, 2009]. The processes by which sediments are transported by the rivers from the eroded regions downstream are complex and not fully understood. They are generally described as a succession of transport, settling, and resuspension cycles. In the three rivers we studied, the most efficient transport occurs during the rainy season when the water level and the water turbulence are high. Not all the particles eroded in the upper reaches of the river are transported to the coast as recently shown by Nie *et al.* [2015] but our results coupled with clay mineralogy and major element content indicate that whatever the number of multiple cycles it has undergone, the magnetic fraction may still represent the lithology of the rocks where it originates from. Indeed, examination of the magnetic properties indicates that their small intrabasin variations are often related to the local geology and in first approximation, they have their counterpart in clay mineralogy and major element content previously published on the same samples and considered at first glance as uniform in each catchment. In detail, the magnetic mineralogy may be even more variable than the clay fraction likely because magnetic minerals are less sensitive to weathering than clays.

On the regional scale, the magnetic properties are variable from one river basin to the other with significant hematite concentration characterizing the sediment from the Mekong river while the Pearl River is characterized by magnetite. The Red river contains some amounts of hematite and locally some sulphides but the magnetic signal remains also dominated by magnetites. This study therefore yields complementary information with respect to the available geochemical and sedimentological data set.

This complementary magnetic data set is now available to decipher the environmental signal from adjacent oceans and in particular the South China Sea in which large amounts of sediment is delivered by these three rivers.

Acknowledgments

This study has been conducted in the framework of the Laboratoire International Associé MONOCL (Monsoon, Ocean and Climate). We are grateful to J. Tarduno and an anonymous referee for their helpful and constructive reviews. Financial support for the analyses performed at LSCE was partly provided by the French INSU/LEFE-MONOCL project. The FORC and low temperature magnetic analyses were performed at the PGL laboratory of the IGG-CAS and supported by the National Natural Science Foundation of China (NSFC grants 41522402 and 41374004) and the Open Project Support from the State Key Laboratory of Lithospheric Evolution (IGGCAS, Beijing). The sampling of river samples was supported by the IOC-WESTPAC FluSed project (South China Sea Fluvial Sediments and Environmental Changes) and the National Natural Science Foundation of China (NSFC grants 91128206 and 91528304). This is LSCE contribution 5726.

References

- An, Z., *et al.* (2015), Global monsoon dynamics and climate change, *Annu. Rev. Earth Planet. Sci.*, *43*, 29–77, doi:10.1146/annurev-earth-060313-054623.
- Clark, M. K., L. M. Schoenbohm, L. H. Royden, K. X. Whipple, B. C. Burchfiel, X. Zhang, W. Tang, E. Wang, and L. Chen (2004), Surface uplift, tectonics and erosion of eastern Tibet from large-scale drainage patterns, *Tectonics*, *23*, TC1006, doi:10.1029/2002TC001402.
- Day, R., M. Fuller, and V. A. Schmidt (1977), Hysteresis properties of titanomagnetite: Grain-size and compositional dependence, *Phys. Earth Planet. Inter.*, *13*, 260–267.
- Duc, D. M., M. T. Nhuan, C. Van Ngoi, T. Nghi, D. M. Tien, T. C. E. van Weering, and G. D. van den Bergh (2007), Sediment distribution and transport at the nearshore zone of the Red River delta, Northern Vietnam, *J. Asian Earth Sci.*, *29*(4), 558–565, doi:10.1016/j.jseas.2006.03.007.
- Dunlop, D. J., and Ö. Özdemir (1997), *Rock Magnetism: Fundamentals and Frontiers*, 573 pp., Cambridge Univ. Press, N. Y.
- Egli, R., A. P. Chen, M. Winklhofer, K. P. Kodama, and C.-S. Horng (2010), Detection of non-interacting single domain particles using first-order reversal curve diagrams, *Geochem. Geophys. Geosyst.*, *11*, Q01Z11, doi:10.1029/2009GC002916.
- Evans, M. E., and F. Heller (2003), *Environmental Magnetism: Principles and Applications of Enviromagnetics*, *Int. Geophys. Ser.*, vol. 86, 299 pp., Academic Press, San Diego, Calif.
- Franke, C., C. Kissel, E. Robin, P. Bonté, and F. Lagroix (2009), Magnetic particle characterization in the Seine river system: Implications for the determination of natural versus anthropogenic input, *Geochem. Geophys. Geosyst.*, *10*, Q08Z05, doi:10.1029/2009GC002544.
- Harrison, R. J., and J. M. Feinberg (2008), FORCinel: An improved algorithm for calculating first-order reversal curve distributions using locally weighted regression smoothing, *Earth Planet. Sci. Lett.*, *171*, 489–502, doi:10.1029/2008GC001987.
- King, J., and J. E. T. Channell (1991), Sedimentary magnetism, environmental magnetism, and magnetostratigraphy, in *U.S. National Report to International Union Geodesy and Geophysics*, *Rev. Geophys. Suppl.*, *29*, 358–370.
- Kissel, C., C. Laj, L. Labeyrie, T. Dokken, A. Voelker, and D. Blamart (1999), Rapid climatic variations during marine isotopic stage 3: Magnetic analysis of North Atlantic sediments, *Earth Planet. Sci. Lett.*, *171*, 489–502.
- Kissel, C., C. Laj, T. Mulder, C. Wandres, and M. Cremer (2009), The magnetic fraction: A tracer of deep water circulation in the North Atlantic, *Earth Planet. Sci. Lett.*, *288*(3–4), 444–454.
- Kissel, C., A. Van Toer, C. Laj, E. Cortijo, and E. Michel (2013), Variations in the strength of the North Atlantic Bottom water during Holocene, *Earth Planet. Sci. Lett.*, *369–370*, 248–259.
- Kruiver, P. P., M. J. Dekkers, and D. Heslop (2001), Quantification of magnetic coercivity components by the analysis of acquisition curves of isothermal remanent magnetisation, *Earth Planet. Sci. Lett.*, *189*, 269–276.
- Liu Y., S. Gao, Y. P. Wang, Y. Yang, J. Long, Y. Zhang, and X. Wu (2014), Distal mud deposits associated with the Pearl River over the north-western continental shelf of the South China Sea, *Mar. Geol.*, *347*, 43–57.

- Liu, Z., and K. Statterger (2014), South China Sea fluvial sediments: An introduction, *J. Asian Earth Sci.*, *79*, 507–508.
- Liu, Z., C. Colin, W. Huang, K. P. Le, S. Q. Tong, Z. Chen, and A. Trentesaux (2007), Climatic and tectonic controls on weathering in South China and the Indochina Peninsula: Clay mineralogical and geochemical investigations from the Pearl, Red, and Mekong drainage basins, *Geochem. Geophys. Geosyst.*, *8*, Q05005, doi:10.1029/2006GC001490.
- Liu, Z., et al. (2016), Source-to-sink processes of fluvial sediments in the South China Sea, *Earth Sci. Rev.*, *153*, 238–273, doi:10.1016/j.earscirev.2015.08.005.
- Mazaud, A., C. Kissel, C. Laj, M. A. Sicre, E. Michel, and J. L. Turon (2007), Variations of the ACC-CDW during MIS3 traced by magnetic grain deposition in midlatitude South Indian Ocean cores: Connections with the northern hemisphere and with central Antarctica, *Geochem. Geophys. Geosystems*, *8*, Q05012, doi:10.1029/2006GC001532.
- Milliman, J. D., and K. L. Farnsworth (2011), *River Discharge to the Coastal Ocean: A Global Synthesis*, 384 pp., Cambridge Univ. Press, Cambridge.
- Milliman J., D., and J. M. P. Syvitski (1992), Geomorphic/tectonic control of sediment discharge to the ocean: The importance of small mountainous rivers, *J. Geol.*, *100*, 525–5441.
- Nesbitt, H. W., and G. M. Young (1982), Early proterozoic climates and plate motions inferred from major element chemistry of lutites, *Nature*, *299*, 715–717.
- Nguyen, T. T. H., W. Zhang, Z. Li, J. Li, C. Ge, J. Liu, X. Bai, H. Feng, and L. Yu (2016), Magnetic properties of sediments of the Red River: Effect of sorting on the source-to-sink pathway and its implications for environmental reconstruction, *Geochem. Geophys. Geosyst.*, *17*, 270–281, doi:10.1002/2015GC006089.
- Nguyen, V. L., T. K. O. Ta, and M. Tateishi (2000), Late Holocene depositional environments and coastal evolution of the Mekong River Delta, Southern Vietnam, *J. Asian Earth Sci.*, *18*, 427–439.
- Nie, J., et al. (2015), Loess Plateau storage of Northeastern Tibetan Plateau-derived Yellow River sediment, *Nat. Commun.*, *6*, 8511, doi:10.1038/ncomms9511.
- Owen, R. B. (2005), Modern fine-grained sedimentation\spatial variability and environmental controls on an inner pericontinental shelf, Hong Kong, *Mar. Geol.*, *214*(1–3), 1–26.
- Ouyang, T., E. Appel, G. Jia, N. Huang, and Z. Zhu (2013), Magnetic mineralogy and its implication of contemporary coastal sediments from South China, *Environ. Earth Sci.*, *68*, 1609–1617, doi:10.1007/s12665-012-1854-1.
- Panagos P., A. Jones, C. Bosco, and P. S. Senthil Kumar (2011), European digital archive on soil maps (EuDASM): Preserving important soil data for public free access, *Int. J. Digital Earth*, *4*(5), 434–443.
- Penny, D. (2006), The Holocene history and development of the Tonle Sap, Cambodia, *Quat. Sci. Rev.*, *25*, 310–322.
- Qin, Y. S. (1963), Preliminary study on submarine relief and sedimentary patterns over the China shelf seas, *Oceanol. Limnol. Sin.*, *5*(1), 71–85.
- Ridd, M. F., A. J. Barber, and M. J. Crow (2011), *The Geology of Thailand*, 626 pp., The Geol. Soc., London, U. K.
- Roberts, A. P., C. R. Pike, and K. L. Verosub (2000), First-order reversal curve diagrams: A new tool for characterizing the magnetic properties of natural samples, *J. Geophys. Res.*, *105*, 28,461–28,475.
- Robertson D. J., and D. E. France (1994), Discrimination of remanence-carrying minerals in mixtures, using isothermal remanent magnetisation acquisition curves, *Phys. Earth Planet. Inter.*, *82*, 223–234.
- Schoenbohm, L., B. C. Burchfiel, L. Chen, and J. Yin (2006), Miocene to present activity along the Red River fault, China, in the context of continental extrusion, upper crustal rotation and lower crustal flow, *Geol. Soc. Am. Bull.*, *118*, 672–688, doi:10.1130/B25816.1.
- Summerfield, M. A., and N. J. Hulton (1994), Natural controls of fluvial denudation rates in major world drainage basins, *J. Geophys. Res.*, *99*, 13,871–13,883.
- Wang, B., LinHo, Y. Zhang, and M. M. Lu (2004), Definition of South China Sea monsoon onset and commencement of the East Asia summer monsoon, *J. Clim.*, *17*, 699–710.
- Wu, Z.-Y., G.-H. Lu, Z.-Y. Liu, J.-X. Wang, and H. Xiao (2013) Trends of extreme flood events in the Pearl River Basin during 1951–2010, *Adv. Clim. Change Res.*, *4*(2), 110–116, doi:10.3724/SP.J.1248.2013.110.
- Xia, X. M., Y. Li, H. Yang, C. Y. Wu, T. H. Sing, and H. K. Pong (2004), Observations on the size and settling velocity distributions of suspended sediment in the Pearl River Estuary, China, *Cont. Shelf Res.*, *24*(16), 1809–1826.
- Zhang, C., and L. Wang (2001), Multi-element geochemistry of sediments from the Pearl River system, China, *Appl. Geochem.*, *16*, 1251–1259.
- Zhang, S. R., X. X. Lu, D. L. Higgitt, C. T. A. Chen, J. T. Han, and H. G. Sun (2008), Recent changes of water discharge and sediment load in the Zhujiang (Pearl River) Basin, China, *Global Planet. Change*, *60*(3–4), 365–380.
- Zhang, W., X. Y. Wei, J. H. Zheng, Y. L. Zhu, and Y. J. Zhang (2012), Estimating suspended sediment loads in the Pearl River delta region using sediment rating curves, *Cont. Shelf Res.*, *38*, 35–46.
- Zhou H., X. Peng, and J. Pan (2004), Distribution, source and enrichment of some chemical elements in sediments of the Pearl River Estuary, China, *Cont. Shelf Res.*, *24*, 1857–1875.